

Nanoscale

Accepted Manuscript



This is an *Accepted Manuscript*, which has been through the Royal Society of Chemistry peer review process and has been accepted for publication.

Accepted Manuscripts are published online shortly after acceptance, before technical editing, formatting and proof reading. Using this free service, authors can make their results available to the community, in citable form, before we publish the edited article. We will replace this *Accepted Manuscript* with the edited and formatted *Advance Article* as soon as it is available.

You can find more information about *Accepted Manuscripts* in the [Information for Authors](#).

Please note that technical editing may introduce minor changes to the text and/or graphics, which may alter content. The journal's standard [Terms & Conditions](#) and the [Ethical guidelines](#) still apply. In no event shall the Royal Society of Chemistry be held responsible for any errors or omissions in this *Accepted Manuscript* or any consequences arising from the use of any information it contains.



Enhanced polarization by coherent heterophase interface between polar and non-polar phase

Gi-Yeop Kim,^{a,b} Kil-Dong Sung,^a Youngmok Rhyim,^a Seog-Young Yoon,^b Min-Soo Kim,^c Soon-Jong Jeong,^c Kwang-Ho Kim,^b Jungho Ryu,^d Sung-Dae Kim^{* a} and Si-Young Choi^{* a}

Received 00th January 20xx,
Accepted 00th January 20xx

DOI: 10.1039/x0xx00000x

www.rsc.org/

A piezoelectric composite containing the ferroelectric polar (Bi(Na_{0.8}K_{0.2})_{0.5}TiO₃: f-BNKT) and the non-polar (0.94Bi(Na_{0.75}K_{0.25})_{0.5}TiO₃-0.06BiAlO₃: BNKT-BA) phases exhibits synergetic properties which combine the beneficial aspects of each phase, i.e., the high saturated polarization (P_s) of the polar phase and the low coercive field (E_c) of the non-polar phase. To understand the origin of such a fruitful outcome from this type of polar/non-polar heterophase structure, comprehensive studies are conducted, including transmission electron microscopy (TEM) and finite element method (FEM) analyses. The TEM results show that the polar/non-polar composite has a core/shell structure in which a polar phase (core) is surrounded by a non-polar phase (shell). In-situ electrical biasing TEM experiments visualize the ferroelectric domains in the polar core are aligned even under an electric field of ~1 kV/mm, which is much lower than its intrinsic coercive field (~3 kV/mm). From the FEM analyses, we can find that the enhanced polarization of the polar phase is promoted by an additional internal field at the phase boundary which originates from the preferential polarization of the relaxor-like non-polar phase. From the present study, we conclude the coherent interface between polar and non-polar phases is a key factor for understanding the enhanced piezoelectric properties of the composite.

Introduction

Piezoelectric materials have been applied in various areas in the electronic industry, including actuators, sensors, generators and transducers.¹⁻⁴ The Pb-based piezoceramics known as PZTs are considered to be the most suitable materials for real-life applications of piezoelectric devices. Nevertheless, Pb-based materials have a fatal weakness in that Pb causes environmental issues. Therefore, Pb-free piezoceramics such as Bi-based composites have attracted much interest as promising candidates for replacing Pb-based materials. Bi-based solid-solution systems such as Bi_{0.5}Na_{0.5}TiO₃ (BNT)-BaTiO₃ (BT), Bi_{0.5}(Na_{1-x}K_x)_{0.5}TiO₃ (BNKT), BNKT-BT, BNKT-BA(BiAlO₃), BNKT-(K_{0.5}Na_{0.5})NbO₃ (KNN) and BNT-BT-KNN are well-known Pb-free piezoelectric materials which have a large electrostrain response as well as a large quality factor compared to the other lead-free piezoelectric oxides. However, these ceramics are not suitable for real-life applications, especially as actuators, because they require a large electric field to be

activated and exhibit hysteretic behavior.⁵⁻²¹ To address these limitations, a great deal of research has been conducted to improve their piezoelectric properties by employing polar (hard or ferroelectric) / non-polar (soft or paraelectric) heterophase composite structures.²²⁻²⁹ With this approach, superior piezoelectric properties such as large electrostrain levels can be realized by coupling the polar and non-polar phases. For example, modified-alkaline niobate (KNN) is a polar/non-polar polycrystalline ceramic composite which shows considerable electrostrain behavior via its unique core (polar)-shell (non-polar) structure.²³ The BNT-based relaxor/ferroelectric composite system (BNT-BT-KNN + BNT-BT) also shows certain advantages via a reduction of the critical electric field to trigger considerable strain by control of the ferroelectric seed composition and the maximum driving field.²⁴ In other Bi-based piezoelectric oxides, polar (f-BNT or f-BNKT) and non-polar (BNKT-BA) composites exhibit significant electrostrain due to the proper remnant polarization (P_r) and coercive field (E_c).²² Furthermore, thin-film systems including the PTO/STO superlattice structure were established to enhance the functional properties of the film using the polar/non-polar heterostructuring concept.²⁵⁻²⁸

However, most works on polar/non-polar phase composites lack explanations of the electrical activation mechanism of each component phase. In order to confirm the polarization behaviors in local dimensions, we performed conventional TEM studies such as dark-field (DF) imaging and selected area diffraction pattern (SADP) analysis. Also, an electric biasing in-situ TEM analysis together with a FEM analysis were performed to reveal the veiled mechanism of polarization

^a Materials Modeling & Characterization Department, Korea Institute of Materials Science, Changwon 642-831, South Korea, E-mail: sdkim@kims.re.kr, youngchoi@kims.re.kr

^b School of Materials Science and Engineering, Pusan National University, Pusan 609-735, South Korea

^c Battery Research Center, Korea Electrotechnology Research Institute, Changwon 641-120, South Korea

^d Functional Ceramics Group, Korea Institute of Materials Science, Changwon 642-831, South Korea

†Electronic Supplementary Information (ESI) available. See DOI: 10.1039/x0xx00000x

behavior in a polar and non-polar composite exhibiting feasible polarization under a low field.

Experimental section

Sample preparation

Polar f-BNKT ($\text{Bi}_{0.5}(\text{Na}_{0.8}\text{K}_{0.2})_{0.5}\text{TiO}_3$) single particles were synthesized by the molten salt method. Bi_2O_3 (Cerac Co., 99.9 %) and TiO_2 (Cerac Co., 99.9 %) powders were reacted in NaCl and KCl (Cerac Co., 99.9 %) flux at 1100 °C for 30 min to obtain plate-like $\text{Bi}_4\text{Ti}_3\text{O}_{12}$ precursor particles. The f-BNKT particles were formed by reacting the plate-like $\text{Bi}_4\text{Ti}_3\text{O}_{12}$, Bi_2O_3 , K_2CO_3 , TiO_2 , and Na_2CO_3 powders in KCl and NaCl flux at 1100 °C for 30 min. After the reactions, the f-BNKT particles were washed in deionized water to remove the residual alkali metal elements and chlorides. Non-polar-phase BNKT-BA ($0.94\text{Bi}_{0.5}(\text{Na}_{0.75}\text{K}_{0.25})_{0.5}\text{TiO}_3-0.06\text{BiAlO}_3$) particles were prepared by the conventional solid-state reaction including the mixing of Bi_2O_3 , Na_2CO_3 , K_2CO_3 , TiO_2 , and Al_2O_3 (99.9 % purity) powders followed by a ball-milling process for 24 hrs in ethanol with zirconia balls. After drying, the mixed powder was calcined at 800 °C. The prepared polar phase and non-polar phase particles were then mixed at a volume ratio of 80 % to 20 % (80 %BNKT-BA+20 %BNKT). The mixed powder was then pressed into a disk (diameter of 12 mm and thickness of 2 mm) and sintered at 1150 °C for 12 hrs. To prevent the evaporation of volatile elements such as Bi, Na, and K during the sintering process, the disk was encapsulated by the precursor powders.

Measurement

The polarization versus electric field (P–E) hysteresis loops were measured using a Precision Premier II (Radiant Technologies, Inc.) device with a frequency of 100 mHz. Field-induced strains were also measured using a contact-type displacement sensor (Millitron 1240) at 50 mHz. TEM samples were prepared by the typical TEM sampling method, including mechanical polishing, dimpling and Ar^+ ion-milling. Before the ion-milling process, the samples were annealed at 250 °C for 30 min to reduce the residual stress which had accumulated during the polishing and dimpling process.

Electrical biasing experiments were conducted with an in-situ electrical biasing TEM holder (JEOL Ltd.). For a proper electrical connection between the sample and the holder, a patterned Al film was deposited on the sample surface and connected to the bias TEM holder through Ag wires (Fig. S1). A sourcemeter (2612B, Keithley) was used as a voltage source of the electrical biasing, and the biasing voltage was controlled by a PC with custom-made software (coded by LabVIEW). The electric field induced on the TEM sample was estimated considering the applied voltage and the patterned gap (100 μm) between the Al electrodes. A TEM (JEOL JEM-2100, JEOL Ltd.) was used for the in-situ experiments and for the microstructural analysis. Real-time video was captured during the in-situ experiment by a CCD camera (Orius 833, Gatan Inc.).

The two-dimensional electric potential distributions in the BNKT-BA mixed composite, under an applied external electric

field, were simulated by a finite-element method (FEM, COMSOL Multiphysics). Electrostatics equations (AC/DC module) were used to calculate the electric charge density

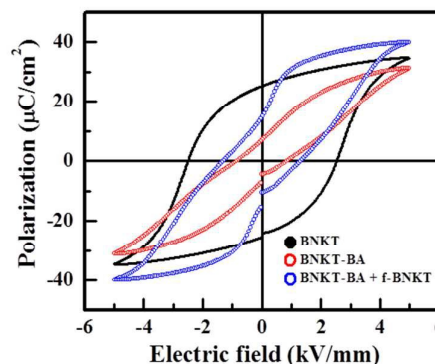


Fig. 1 Polarization-electric field curves of BNKT, BNKT-BA, BNKT-BA + f-BNKT samples, as plotted by the black dots, red circles, and blue circles, respectively

concerning the relative permittivity (ϵ_r) of the component phases only ($\rho_v = \nabla \cdot \epsilon_0 \epsilon_r E$) or ϵ_r with remnant electric displacement of the BNKT-BA shell phase ($\rho_v = \nabla \cdot \epsilon_0 \epsilon_r E + D_r$).

Results and discussion

Fig. 1 shows the polarization hysteresis loops (polarization (P) versus the electric field (E) curve, P–E curve) of the Bi-based ceramic composites, i.e., BNKT, BNKT-BA and BNKT-BA + f-BNKT. The P–E curve of the BNKT sample (denoted by the black filled circles) exhibits a typical ferroelectric (polar) hysteresis feature, i.e., large values of the electric coercive field (E_c) and remnant polarization (P_r). On the other hand, the P–E curve of the BNKT-BA composite (denoted by the red empty circles) has lower values of E_c , P_r and the saturated polarization (P_s), indicative of the piezoelectric relaxor-like (non-polar) nature of the BNKT-BA composite.⁷ On the other hand, the BNKT-BA + f-BNKT composite shows a large P_s value and a small E_c value, coupled polarization behavior between the non-polar phase and the polar phase, as indicated by the empty blue circles in Fig. 1. Furthermore, this coupled polarization feature, shown in Fig. S2, is known to give rise to the considerable amount of electrostrain behavior found in composite ferroelectric ceramics.^{2, 12–15, 22, 23}

At first glance, the polarization behavior of the BNKT-BA + f-BNKT composite can be understood by considering the coercive field value of the f-BNKT polar phase (3 kV/mm) and the BNKT-BA non-polar phase (0.8 kV/mm). The slope of the P–E curve at the initial electric poling process is likely to be dependent on the non-polar phase because the polar phase cannot be activated in such a low field. However, it is apparent that the slope of the P–E curve in the low-field region was increased slightly by the addition of f-BNKT, implying that the polar f-BNKT already has some effect on the initial polarization behavior of the BNKT-BA + f-BNKT composite. In other words, the increased slope at ~ 1 kV/mm in the P–E curve of the polar and non-polar composite may be related to

activation of the f-BNKT polar phases, but the single phase of f-BNKT cannot be polarized at such a low electric field. To this end, we investigated the enhanced polarization behavior,

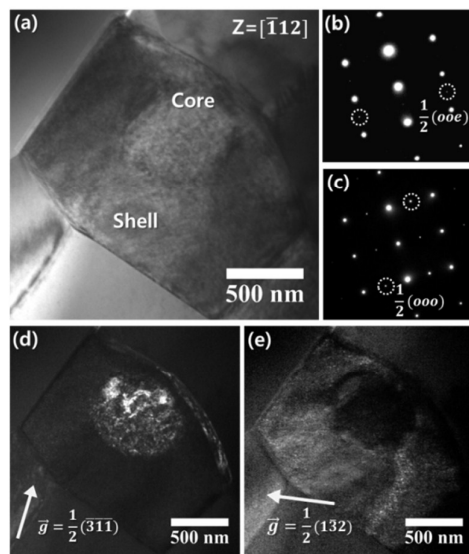


Fig. 2 TEM micrographs of a core-shell type grain in a BNKT-BA + f-BNKT composite. (a) Bright-field (BF) image of the core-shell grain, (b) and (c) SAED patterns of the shell (BNKT-BA) and core (f-BNKT) regions with the $[112]$ zone-axis, respectively. (d) and (e) Centered dark-field (CDF) images of the core (f-BNKT) and shell (BNKT-BA) regions with $\vec{g} = \frac{1}{2}(311)$ and $\vec{g} = \frac{1}{2}(132)$, respectively. Most of the grains in BNKT-BA + f-BNKT are composed of the f-BNKT core and the BNKT-BA shell.

especially focusing on the activation of the polar phase in the initial poling state, by means of a microstructural analysis.

From the TEM observations, the BNKT-BA + f-BNKT polycrystalline composite was found to exhibit two different types of grains. The first is the single-phase grain shown in Fig. S3, where the superlattice spots in the corresponding SADP are indexed as $1/2(o\bar{o}o)$ (noted that ‘o’ and ‘e’ represent odd and even Miller indices, respectively). Because this type of superlattice spot can be generated from the in-phase ($a^0a^0c^+$) octahedral tilt symmetry in space group of $P4bm$,^{15, 30-37} these grains are found to be composed of the non-polar BNKT-BA phase. Most of the grains in the BNKT-BA + f-BNKT polycrystalline composite have a core-shell structure, as clearly displayed in Fig. 2a. The SADP taken from the shell region (Fig. 2b) also contains the $1/2(o\bar{o}e)$ superlattice spots, indicating that the shell region is composed of the non-polar BNKT-BA phase (tetragonal $P4bm$). At the core region, however, different superlattice spots are shown in the SADP (Fig. 2c), specifically $1/2(o\bar{o}o)$ spots. As electron diffraction spots which have a Miller index of $1/2(o\bar{o}o)$ can originate from the anti-phase ($a^+a^+a^+$) tilt symmetry in a perovskite,^{15, 30-37} the core region is composed of the rhombohedral ($R3c$) polar phase, i.e., the f-BNKT phase. It should be noted that the added f-BNKT particles emerged into the core phases during the sintering process. This can be attributed to the crystallographic

and compositional isotropy between the BNKT-BA and the f-BNKT phases. Dark-field (DF) TEM images taken by selecting the superlattice spots of the $1/2(o\bar{o}o)$ from the core (Fig. 2d) and the $1/2(o\bar{o}e)$ from the shell region (Fig. 2e) also clearly confirm the location of the polar core (rhombohedral, f-BNKT) and non-polar shell (tetragonal, BNKT-BA). The TEM results also demonstrate that the BNKT-BA + f-BNKT polycrystalline composite mostly consists of the core-shell structure and that the polar phase (f-BNKT) remains in a grain as a core phase with the non-polar matrix phase (BNKT-BA).

Next, we visualized the polarization behavior of the core-shell type grains by the in-situ TEM technique. Electric biasing in-situ TEM microscopy, enabling the observation of microstructural changes in real time along with external electric stimuli, has been considered as a useful tool for understanding the polarization mechanism of composite piezoceramics.³⁵⁻³⁷ Bright-field TEM images of the mixed grain were taken under a different applied electric field, maintaining the $g(100)$ two-beam condition to illustrate the ferroelectric domain structure more clearly. In the absence of an external electric field (Fig. 3a), consistent with Fig. 2b-e, the grain has a non-polar shell with a single domain and a polar core with multiple domains. When the applied electric field was increased up to 2 kV/mm (Fig. 3b-c), domain switching at the core region was observed; domain boundaries in the core region, clearly seen at the zero field, disappeared as the electric field was increased. After removing the electric field (Fig. 3d), the domain structure recovered to its initial state. In terms of phase stability, we could not find any evidence of phase transitions because there was no change in the SADPs (Fig. 3e-g) from the core region. Interestingly, it is generally accepted that this reversible domain switching behaviour of the f-BNKT phase cannot take place within such a low-field region below the coercive field of f-BNKT (3 kV/mm).

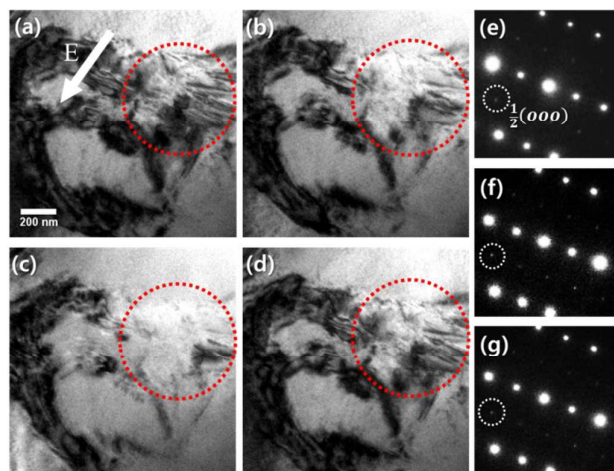


Fig. 3 TEM micrographs of a core-shell type grain when an external electric field of (a) 0 kV/mm (b) 1 kV/mm, and (c) 2 kV/mm was applied. (d) TEM image after removing the external electric field. SADPs taken in the core region with the z zone-axis (e) at 0 kV/mm, (f) at 2 kV/mm and (g) after removing the external electric field. The core region is highlighted by the red dotted circle.

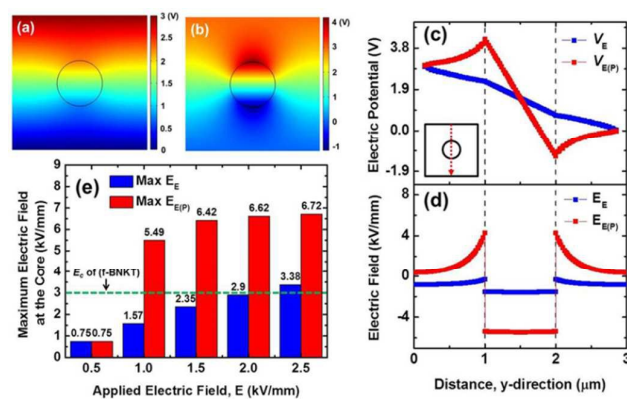


Fig. 4 Two-dimensional electric potential distribution maps under an external field of 1 kV/mm, considering (a) ϵ_r only ($\rho_v = \nabla \cdot \epsilon_0 \epsilon_r E$) and (b) ϵ_r with the generated electric charges in the shell phase ($\rho_v = \nabla \cdot \epsilon_0 \epsilon_r E + D_r$). (c) Electric potential and (d) electric field profiles along the centered vertical line in the 2-D model. (e) Calculated maximum electric field values at the core phase as a function of the externally applied electric field considering ϵ_r only (blue bars) and ϵ_r with the activated electric charges in the shell phase (red bars).

To explain this unexpected phenomenon, we conducted simple numerical calculations considering a unique intragranular heterostructure containing a polar core and non-polar shell.

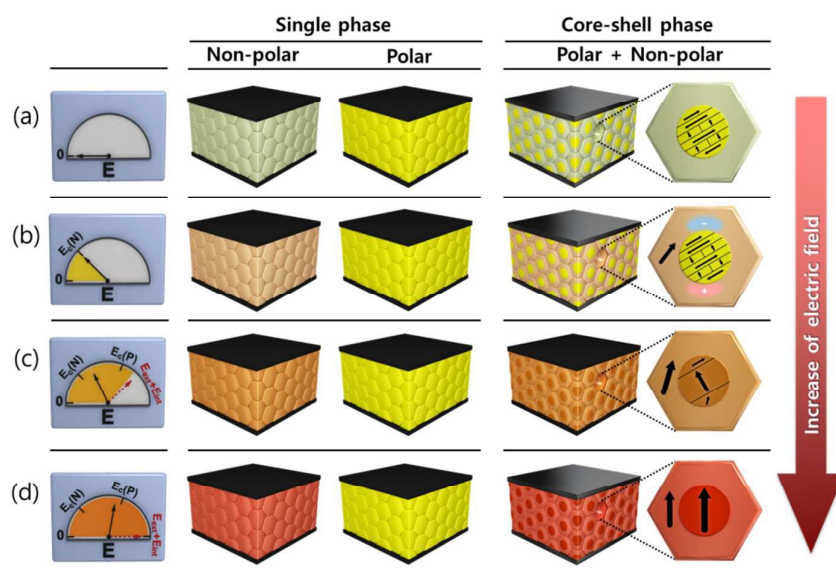
First, the relative permittivity (ϵ_r) of each polar and non-polar phase was considered. To evaluate the effects of ϵ_r on the electric potential distribution in the mixed composite when an external electric field was applied, a simple two-dimensional model system was built and analyzed by a modeling tool (COMSOL Multiphysics). To mimic the mixed composite structure, the model contained a circular core phase (diameter of 1 μm) within a square-shaped shell phase (3 μm \times 3 μm). Regarding our material system, it was reported in the literature that the ϵ_r value of the *P4bm* non-polar phase (BNKT-BA) is larger than that of the *R3c* polar phase (f-BNKT) within a low electric field range (~ 3 kV/mm); the ϵ_r values of the BNKT-BA and f-BNKT phase are 3346 and 710 at 1 kV/mm, respectively.²² Fig. 4a shows the calculated electric potential distribution of the model system when an external electric field of 1 kV/mm was applied between the upper (+3 V) and lower (grounded) end boundary. The line profile of the electric potential along the y-direction (the blue line in Fig. 4c) reveals that the electric potential contour was deflected at the phase boundary, meaning that a more intense electric field was induced on the core phase (the blue line in Fig. 4d). However, the maximum value of the field induced in the core phase was calculated to be 1.57 kV/mm, which is not sufficient to polarize the core polar phase; the value is lower than that of the coercive field (3 kV/mm) of the f-BNKT. As the effects of the ϵ_r difference between the core and shell phase cannot fully explain the experimental observations, we therefore must seek another possibility along with the electric permittivity to explain the polarization behavior of the core f-BNKT phase under a low field.

The BNKT-BA non-polar phase has a piezoelectric relaxor-like property and a low coercive field value (0.8 kV/mm), meaning that the BNKT-BA phase can be easily polarized even when a

low electric field is applied. Then, electric charges, caused by the remnant electric displacement (D_r) of the polarized BNKT-BA phase, are accumulated at the phase boundary between the non-polar BNKT-BA and the polar f-BNKT. We calculated the electric field distribution (Fig. 4b) of the model system with an external field of 1 kV/mm considering the remnant electric charges (D_r : 0.161 C/m²) in the BNKT-BA shell phase. In this case, the electric potential distribution contours were severely deflected at the phase boundary, with the result that the maximum (+4.21 V) and minimum (-1.21 V) electric potentials were created at the boundary (the red line in Fig. 4c). Therefore, the slope of the electric potential along the direction of the external applied field, and the induced electric field at the core, were also increased (the red line in Fig. 4d). The maximum value of the induced electric field in the polar core phase was calculated to be 5.49 kV/mm. As a result, the provided electric field in the core region became large enough to induce the domain switching (polarization) of the polar f-BNKT core.

Furthermore, we calculated the maximum electric field values induced at the core polar phase as a function of the external electric field (Fig. 4e). For calculations (the blue bars in Fig. 4e) considering ϵ_r only ($\rho_v = \nabla \cdot \epsilon_0 \epsilon_r E$), the maximum electric field at the core phase did not exceed its E_c value (3 kV/mm) until the external field reached 2.5 kV/mm. However, considering the remnant electric charges in the BNKT-BA shell phase ($\rho_v = \nabla \cdot \epsilon_0 \epsilon_r E + D_r$), the calculated maximum electric field at the core reached 5.49 kV/mm even at an external field of 1 kV/mm. From these calculations, we could confirm that the remnant electric displacement at the core-shell phase boundary, provided by the polarization of the non-polar shell, plays a critical role in the polarization of the hard ferroelectric phase, even at such a low applied electric field.

Fig. 5 concisely illustrates the proposed polarization mechanism of the polar–non-polar composite. Without the external electric field (Fig. 5a), there remains hardly any remnant polarization in the shell phase (non-polar), whereas the core phase has remnant polarization (polar) in the form of multiple ferroelectric domains. In the initial polling state (Fig. 5b), the ferroelectrically susceptible shell phase (soft ferroelectric, non-polar phase) would be polarized by a low external field, after which the additional electric charges accumulate at the phase boundary, giving rise to an internal electric field to the core phase. Then, this effective field induced on the core phase, the sum of the external electric field and the internal electric field, becomes enough high to overcome the critical value (coercive field, E_c) eligible for the ferroelectric domain switching of the core phase (Fig. 5c). After activating the core phase, the total polarization behavior of the polar/non-polar composite follows that of the ferroelectrically hard core phase (Fig. 5d). When the external electric field is removed, remnant electric polarization of polar phase produces another internal electric field with the opposite direction to the external electric field, and acts as a restoring force to make polar phase be initial state by accompanying reversed electric polarization of non-polar phase.³⁸ (Fig. S5)



Finally, it is also important to note the importance of the core-shell heterophase structure can be used to enhance the properties of

Fig. 5 Schematic illustrations of the poling processes of the single phases and core-shell phase composites when (a) E_{ext} (the externally applied electric field) = 0kV/mm (b) $E_c(P) > E_{\text{ext}} > E_c(N)$ (c) $E_c(P) \geq E_{\text{ext}}$ and (d) $E_{\text{ext}} > E_c(P)$. $E_c(P)$ and $E_c(N)$ represent the coercive field of the polar core phase and the non-polar shell phase, respectively.

shell structure itself on the polarization of the hard ferroelectric phase (f-BNKT) at such a low electric field. In the event that the polar and non-polar phases have their own single grains and thus the two phases are separated by grain boundaries, the surface charges created by the polarization of the easy polarizable phase (the non-polar phase) will leak through the grain boundary, leaving no significant internal electric fields. With the coherent nature of the interface between the core and shell phase, furthermore, strain and other structural defects (dislocations or point defects, etc.) near the interface can also influence the domain switching behaviour.⁴⁰⁻⁴³ Therefore, according to our results, it is convincing that the ferroelectric properties of composite ceramics also can be tuned by controlling the intragranular core-shell structure and by selecting the component phases.

Conclusions

In summary, we investigated the electric polarization behaviors of Bi-based piezoelectric composite ceramics (BNKT, BNKT-BA and BNKT-BA + f-BNKT), specifically in a polar and non-polar polycrystalline composite (BNKT-BA + f-BNKT). TEM analyses combined with in-situ electric biasing TEM experiments visualized the ferroelectric domain switching of the polar phase (f-BNKT) under a low external field (1 kV/mm). We propose that the activated electric displacement at the phase boundary, generated by the polarization of the non-polar (soft ferroelectric) phase in the heterophase structure, is the main origin of the unexpected polarization behavior of the polar (hard ferroelectric) phase in the BNKT-BA + f-BNKT composite. It is also noteworthy that the intragranular

piezoelectric ceramics.

Acknowledgements

This research was supported by the Global Frontier Program through the Global Frontier Hybrid Interface Materials (GFHIM) of the National Research Foundation of Korea (NRF) funded by the Ministry of Science, ICT & Future Planning (2013M3A6B1078872).

References

- 1 J. Rödel, W. Jo, K. T. Seifert, E. Anton, T. Granzow and D. Damjanovic, *J. Am. Ceram. Soc.*, 2009, **92**, 1153.
- 2 W. Jo, R. Dittmer, M. Acosta, J. Zang, C. Groh, E. Sapper, K. Wang and J. Rödel, *J. Electroceram.*, 2009, **29**, 71.
- 3 D. H. Seol, H. Taniguchi, J. Y. Hwang, M. Itoh, H. J. Shin, S. W. Kim and Y. S. Kim, *Nanoscale*, 2015, **7**, 11561.
- 4 Z. Li, G. Zhu, R. S. Yang, A. C. Wang and Z. L. Wang, *Adv. Mater.*, 2010, **22**, 2534.
- 5 N. Liu, R. Dittmer, R. W. Stark and C. Dietz, *Nanoscale*, 2015, **7**, 11787.
- 6 A. Ullah, C. W. Ahn, K. B. Jang, A. Hussain and I. W. Kim, *Ferroelectrics.*, 2010, **404**, 167.
- 7 A. Ullah, C. W. Ahn, A. Hussain, S. Y. Lee and I. W. Kim, *J. Am. Ceram. Soc.*, 2011, **94**, 3915.
- 8 A. Sasaki, T. Chiba, Y. Mamiya and E. Otsuki, *Jpn. J. App. Phys.*, 1999, **38**, 5564.
- 9 K. Yoshii, Y. Hiruma, H. Nagata and T. Takenaka, *J. App. Phys.*, 2006, **45**, 4493.
- 10 Y. Hiruma, K. Yoshii, H. Nagata and T. Takenaka, *Ferroelectrics.*, 2007, **346**, 114.
- 11 Y. Hiruma, H. Nagata and T. Takenaka, *J. Appl. Phys.*, 2008, **104**, 124106.

- 12 J. Hao, B. Shen, J. Zhai, C. Liu, X. Li and X. Gao, *J. Appl. Phys.*, 2013, **113**, 114106.
- 13 J. Hao, W. Bai, W. Li, B. Shen and J. Zhai, *J. Appl. Phys.*, 2013, **114**, 044103.
- 14 R. Dittmer, W. Jo, J. Rödel, S. Kalinin and N. Balke, *Adv. Funct. Mater.*, 2012, **22**, 4208.
- 15 S. Cheng, J. Shieh, H. Lu, C. Shen, Y. Tang and N. Ho, *J. Eur. Ceram. Soc.*, 2013, **33**, 2141.
- 16 L. A. Schmitt, J. Kling, M. Hinterstein, M. Hoelzel, W. Jo, H. Kleebe and H. Fuess, *J. Mater. Sci.*, 2011, **46**, 4368.
- 17 W. Jo, T. Granzow, E. Aulbach, J. Rödel and D. Damjanovic, *J. Appl. Phys.*, 2009, 105, 094102.
- 18 S. Zhang, A. B. Kounga, E. Aulbach, H. Ehrenberg and J. Rödel, *Appl. Phys. Lett.*, 2013, **91**, 112906.
- 19 S. Zhang, A. B. Kounga, E. Aulbach, W. Jo, T. Granzow, H. Ehrenberg and J. Rödel, *J. Appl. Phys.*, 2008, **103**, 034108.
- 20 S. Zhang, A. B. Kounga, E. Aulbach, T. Granzow, W. Jo, H. Kleebe and J. Rödel, *J. Appl. Phys.*, 2008, **103**, 034107.
- 21 Y. Guo, Y. Liu, R. L. Withers, F. Brink and H. Chen, *Chem. Mater.*, 2010, **23**, 219.
- 22 D. S. Lee, S. J. Jeong, M. S. Kim and J. H. Koh, *J. Appl. Phys.*, 2012, **112**, 124109.
- 23 S. Choi, S. Jeong, D. Lee, M. Kim, J. Lee, J. H. Cho, B. I. Kim and Y. Ikuhara, *Chem. Mater.*, 2012, **24**, 3363.
- 24 C. Groh, D. J. Franzbach, W. Jo, K. G. Webber, J. Kling, L. A. Schmitt, H. Kleebe, S. Jeong, J. Lee and J. Rödel, *Adv. Funct. Mater.*, 2014, **24**, 356.
- 25 M. Dawber, C. Lichtensteiger, M. Cantoni, M. Veithen, P. Ghosez, K. Johnston, K. Rabe and J. Triscone, *Phys. Rev. Lett.*, 2005, **95**, 177601.
- 26 P. Zubko, N. Jecklin, A. Torres-Pardo, P. Aguado-Puente, A. Gloter, C. Lichtensteiger, J. Junquera, O. Stéphan and J. Triscone, *Nano Lett.*, 2012, **12**, 2846.
- 27 P. Zubko, N. Stucki, C. Lichtensteiger and J. Triscone, *Phys. Rev. Lett.*, 2010, **104**, 187601.
- 28 P. Aguado-Puente, P. Garcia-Fernandez and J. Junquera, *Phys. Rev. Lett.*, 2011, **107**, 217601.
- 29 J. Y. Li, R. C. Rogan, E. Üstündag and K. Bhattacharya, *Nat. Mat.*, 2005, **4**, 776
- 30 A. Glazer, *Acta Crystallographica Section B: Structural Crystallography and Crystal Chemistry.*, 1972, **28**, 3384.
- 31 P. M. Woodward, *Acta Crystallographica Section B: Structural Science.*, 1997, **53**, 32.
- 32 V. Dorcet and G. Trolliard, *Acta Materialia*, 2008, **56**, 1753.
- 33 C. W. Tai and Y. Lereah, *Appl. Phys. Lett.*, 2009, **95**, 062901.
- 34 D. I. Woodward and I. M. Reaney, *Acta Crystallographica Section B: Structural Science.*, 2005, **61**, 387.
- 35 C. Ma, H. Guo, S. P. Beckman and X. Tan, *Phys. Rev. Lett.*, 2012, **109**, 107602.
- 36 X. Tan, C. Ma, J. Frederic, S. Beckman and K. G. Webber, *J. Am. Ceram. Soc.*, 2011, **94**, 4091.
- 37 J. Kling, X. Tan, W. Jo, H. Kleebe, H. Fuess and J. Rödel, *J. Am. Ceram. Soc.*, 2010, **93**, 2452.
- 38 F. Kagawa, S. Horiuchi, N. Minami, S. Ishibashi, K. Kobayashi, R. Kumai, Y. Murakami and Y. Tokura, *Nano Lett.*, 2015, **14**, 239.
- 39 X-Q. Fang, J-X Liu and V. Gupta, *Nanoscale*, 2013, **5**, 1716.
- 40 X. Ren, *Nat. Mater.*, 2004, **3**, 91.
- 41 C. T. Nelson, P. Gao, J. R. Jokisaari, C. Heikes, C. Adamo, A. Melville, S.-H. Baek, C. M. Folkman, B. Winchester, Y. Gu, Y. Liu, K. Zhang, E. Wang, J. Li, L.-Q. Chen, C.-B. Eom, D. G. Schlom and X. Pan, *Science*, 2011, **334**, 968.
- 42 J. K. Lee, G. Y. Shin, K. Song, W. S. Choi, Y. A. Shin, S. Y. Park, J. Britson, Y. Cao, L. Q. Chen, H. N. Lee and S. H. Oh, *Acta Mater.*, 2013, **61**, 6765.
- 43 T. H. Kim, B. C. Jeon, T. Min, S. M. Yang, D. S. Lee, Y. S. Kim, S. H. Baek, W. Saenrang, C. B. Eom, T. K. Song, J. G. Yoon and T. W. Noh, *Adv. Funct. Mater.*, 2012, **22**, 4962.